Linking Excess Entropy and Acentric Factor in Spherical Fluids

Tae Jun Yoon[1, 2] and Ian H. Bell[3]

[1)] *School of Transdisciplinary Innovations, Seoul National University, Seoul, 08826, Republic of Korea*

[2)] *School of Chemical and Biological Engineering, Institute of Chemical Processes, Seoul National University, Seoul, 08826, Republic of Korea*[a)]

[3)] *Applied Chemicals and Materials Division, National Institute of Standards and Technology, Boulder, 80305, Colorado, United States*[b)]

(Dated: 13 August 2024)

Introduced by Pitzer in 1955, the acentric factor (ω) has been used to evaluate a molecule's deviation from the corresponding state principle. Pitzer devised ω based on a concept called *perfect liquid* (or centric fluid), a hypothetical species perfectly adhering to this principle. However, its physical significance remains unclear. This work attempts to clarify the centric fluid from an excess entropy perspective. We observe that the excess entropy per particle of centric fluids approximates $-k_{\mathrm{B}}$ at their critical points, akin to the communal entropy of an ideal gas in classical cell theory. We devise an excess entropy dissection and apply it to model fluids (square-well, Lennard-Jones, Mie n-6, and the two-body ab initio models) to interpret this similarity. The dissection method identifies both centricity-independent and dependent entropic features. Regardless of the acentric factor, the attractive interaction contribution to the excess entropy peaks at the density where local density is most enhanced due to the competition between the local attraction and critical fluctuations. However, only in centric fluids does the entropic contribution from the local attractive potential become comparable to that of the hard sphere exclusion, making the centric fluid more structured than acentric ones. These findings elucidate the physical significance of the centric fluid as a system of particles where the repulsive and attractive contributions to the excess entropy become equal at its gas-liquid criticality. We expect these findings to offer a way to find suitable intermolecular potentials and assess the physical adequacy of equations of state.

[a)]Electronic mail: tyoon124@snu.ac.kr
[b)]Electronic mail: ian.bell@nist.gov

I. INTRODUCTION

The principle of corresponding states, initially proposed by van der Waals in 1873,[1] describes that all fluids have approximately the same deviation from the ideal gas behavior at the same reduced temperature ($T_\mathrm{r} \equiv T/T_\mathrm{crit}$) and pressure ($p_\mathrm{r} \equiv p/p_\mathrm{crit}$). Although this approach helped outline the universality of critical phenomena and has been widely used to correlate thermophysical properties of fluid systems, it does not quantitatively reproduce the non-ideal behavior of all fluids. Hence, pioneers in theoretical chemistry and chemical thermodynamics extensively explored the non-corresponding state behavior of molecular fluids.[2–4]

One of the pioneers, Kenneth Pitzer, suggested a conceptual species called *perfect liquid*[3] obeying the corresponding state principle. He proposed that this species should satisfy the following hypotheses.[3]

H1 The molecules obey classical statistical mechanics.

H2 Molecules are spherically symmetrical. This statement does not necessarily exclude polyatomic species. A molecule is considered spherically symmetrical if it rotates rapidly and freely.

H3 Intramolecular vibration does not change depending on thermodynamic conditions.

H4 The potential energy of a molecule depends only on the intermolecular distances between the molecule and its neighbors.

H5 The potential energy for a pair of molecules is written as $\phi = A\varphi(r/r_0)$ where φ is a universal function, r is the intermolecular distance, and r_0 and A are molecular parameters.

To avoid the impression that *perfect liquid* denotes a liquid state, we will refer to it as a centric fluid throughout this work. Based on experimental observations, Pitzer expected that the vapor pressure of centric fluids should be higher than acentric ones. He then defined the acentric factor to quantify the deviation from the corresponding state principle in terms of the vapor pressure, which is given as[5]

$$\omega = -\log_{10} p_\mathrm{r}(T_\mathrm{r} = 0.7) - 1.0 \tag{1}$$

where the reduced saturation pressure is determined at the reduced temperature of $T_{\mathrm{r}} = 0.7$. The acentric factor becomes approximately zero for centric fluids (e.g., argon, krypton, and xenon). For its convenience of calculation (based on readily accessible experimental data), ω has been widely utilized as a standard thermophysical property for modeling the behavior of fluid systems.

Despite its usefulness, however, understanding the physical significance of centric fluid is still elusive from a physical point of view. Guggenheim has already criticized some ambiguities in the ansatzes H1–H5 in defining the centric fluid.[4] However, it would be helpful to re-examine these statements carefully. Hypothesis H1 excludes quantum fluids (e.g., hydrogen and helium), but some molecules (e.g., neon) are located at the boundary between the quantum fluid and the classical one. Guggenheim states that Hypothesis H2 allows some diatomic and polyatomic molecules in gas and liquid states to be included as centric fluids. In his later work,[6] Pitzer also states that a molecule is considered centric if the intermolecular forces induced by non-centric parts are insignificant. For instance, CH_4 is considered centric, while *n*-propane is not; the *spherical symmetry* is determined not by the molecular shape but by a complex effect of both molecular shape and interatomic forces, which is challenging to quantify. Hypotheses H3, H4, and H5 rule out strongly polar or hydrogen bonding substances. However, as Guggenheim states, no *a priori* justification exists for hypothesis H5. Pitzer expected that no real molecule would exactly satisfy the last condition. However, he speculated that the interatomic potential $\phi(r)$ of a centric fluid would follow the inverse sixth power law $\phi(r) = Cr^{-6}$, while its repulsive part would not affect the corresponding state behavior significantly.

Indeed, hypothesis H5 raises several questions regarding the nature of centric fluids. A number of studies published after the introduction of ω demonstrate that the nature of $\phi(r)$ significantly impacts the thermophysical properties of fluid systems. For instance, classical perturbation theory states that the repulsive part dominantly determines the liquid structure.[7] Then, why is the inverse sixth power law necessary to satisfy $\omega = 0$? How does the steepness (or reach) of the repulsive (or attractive) interactions affect the acentric factor? All things considered, Pitzer's hypotheses are helpful in ruling out some molecules from the list of centric fluids and getting an inkling of what the centric fluid should be, but cannot be used to derive a solid definition.

In addition to these questions, understanding the physical significance of the centric fluid

based on Eq. 1 is challenging. The reference temperature $T_r = 0.7$ was arbitrarily chosen considering the data availability while avoiding the critical anomalies; the absolute magnitude of the acentric factor does not have a physical significance.[6] Moreover, the reference temperature is problematic for some substances, such as SF_6 and CO_2, as their reference temperatures ($T_r = 0.7$) are below their triple points.[8] Lastly, no structural insight is obtained from Eq. 1.

This work tests if the excess entropy can work as a key to elucidate the physical nature of the centric fluid. Excess entropy per particle is defined as the extent of deviation from its ideal gas state at the same density and temperature ($s_{ex} = [S(\rho, T) - S_{ig}(\rho, T)]/N$).[9] This term is also called as the residual entropy in physical chemistry.[10] Since most systems are more *ordered* than the ideal gas, s_{ex} is negative in most fluids, except for exotic systems like Fermi-Dirac fluids. For brevity, we use a dimensionless variable s^+ defined as $s^+ \equiv -s_{ex}/k_B$ so that the order parameter s^+ is positive and converges to zero at the low-density limit. The dimensionless quantity s^+ has been linked with transport properties,[11,12] thermodynamic properties[13], dynamic crossover,[14,15] and phase equilibria.[16–18]

Although not systematically performed, several earlier studies explored an empirical (or semi-empirical) link between s_{ex} and ω. By examining the attractive tail of the Kihara potential, Pitzer expected that the magnitude of excess entropy should be lowest in the centric molecule compared to acentric ones.[19] Bell showed that the critical excess entropy calculated using the Peng-Robinson equation of state (EOS) is a linear function of the acentric factor.[20] Using the density scaling approach, which is closely related to the excess entropy scaling approach,[21] Fragiadakis and Roland[22] showed that the density scaling exponent γ matches with the scaling exponent for the melting point Γ only in the centric fluids. Lastly, some (semi-)empirical correlations were proposed to calculate transport properties combining the excess entropy scaling approach and thermodynamic EOSs.[23,24]

II. EMPIRICAL OBSERVATIONS

Our curiosity about the relationship between ω and s_{ex} stems from an empirical observation that the dimensionless quantity s^+ at the gas-liquid critical point ($s^+_{crit} \equiv -s_{ex,crit}/k_B$) is close to unity for noble gases, except for helium-4 (^{4}He), and to a lesser extent for neon (Figure 1a). Although real ^{4}He is influenced by strong quantum effects at its critical point,

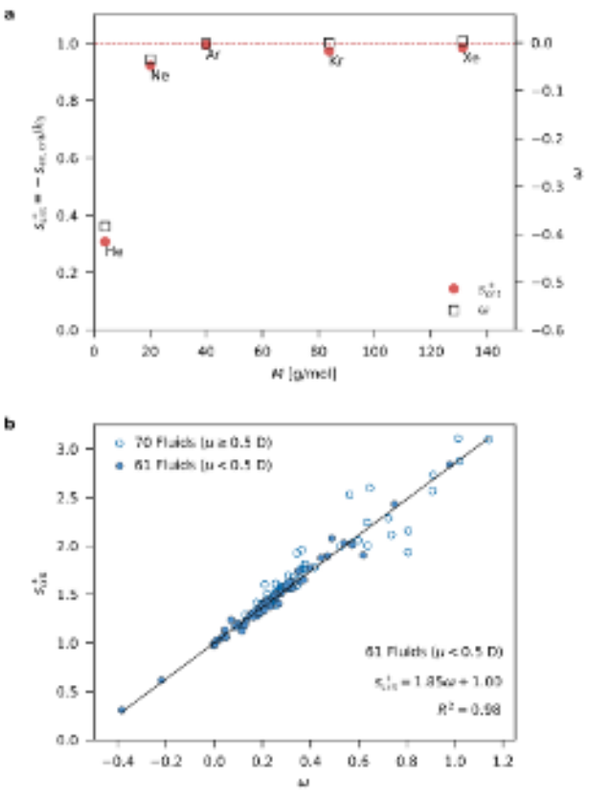

FIG. 1. Empirical observations about the relationship between s^+ at the critical point (s^+_{crit}) and ω from the NIST thermophysical properties database. **a** The values of s^+ of noble gases at their gas-liquid critical points. As the molecular weight increases, the quantum effect is reduced, and s^+_{crit} converges to unity. When the quantum effect is excluded, the s^+_{crit} becomes close to unity. **b** Correlation between the acentric factors (ω) and s^+_{crit}. When a simple linear relation is assumed, s^+_{crit} becomes 1.00 ± 0.04 at $\omega = 0$ when non-polar or weakly polar substances are used for the regression (61 fluids). For 135 fluids in the NIST REFPROP, the empirical linear model yields $s^+_{\mathrm{crit}}(\omega = 0) = 1.02 \pm 0.05$.

thermophysical properties of classical ^{4}He without the nuclear quantum effect are available.[25,26] When the virial coefficients are used, $s^+_{\mathrm{crit}} = 1.0 \pm 0.02$ is obtained for classical ^{4}He; quantum effects reduce s^+_{crit} (See Sec. S1 in Supplementary Material for the detailed calculation results). Hence, the excess entropy of all noble gases becomes close to $-k_{\mathrm{B}}$ at their gas-liquid critical points when the quantum effect is excluded.

We further examine the relationship between ω and s^+_{crit} for 135 fluids in the NIST

REFPROP library.[8] The fluids covered in NIST REFPROP are well-measured molecules for which high-accuracy EOSs are available, covering a variety of chemical species. Following hypotheses H3–H5 and the Peng-Robinson EOS behavior,[20] we first apply a simple linear model ($s^+_{\rm crit} = a\omega + b$) to 61 non-polar fluids whose dipole moments are less than 0.5 D, although this threshold is somewhat arbitrary. The model yields $s^+_{\rm crit} = 1.00 \pm 0.04$ at $\omega = 0$ ($R^2 = 0.98$). (Figure 1b) Interestingly, when the model is applied to all 135 fluids, the goodness of fit is decreased from 0.98 to 0.95, but the $s^+_{\rm crit}$ value of the centric fluid is still close to unity ($s^+_{\rm crit} = 1.02 \pm 0.05$).

III. THEORETICAL INTERPRETATIONS

The link between $s^+_{\rm crit} = 1$ and $\omega = 0$ discovered in Sec. II reminds us of the classical cell theory, one of the earliest models to understand liquid thermodynamics.[27] In the cell theory, the thermophysical properties of a system are calculated, assuming that molecules independently move inside their cells. This hypothesis makes it easy to calculate the thermophysical properties of liquids but causes an artifact called communal entropy.[28] For instance, in an ideal gas system where molecules freely move, the dimensionless entropy per particle is calculated as

$$\frac{S_{\rm ig}}{Nk_{\rm B}} = \frac{5}{2} + \ln\left(\frac{V}{N\Lambda^3}\right) \tag{2}$$

where N is the number of particles, V is the system volume, and Λ is the thermal de Broglie wavelength. When ideal gas molecules are only allowed to move in their cells, the entropy per particle is obtained as

$$\frac{S_{\rm cell}}{Nk_{\rm B}} = \frac{3}{2} + \ln\left(\frac{v}{\Lambda^3}\right) \tag{3}$$

Here, the cell size is assumed to be $v = V/N = \rho^{-1}$. By subtracting Eq. 2 from Eq. 3, the dimensionless entropy change is obtained as $-(S_{\rm cell} - S_{\rm ig})/Nk_{\rm B} = -s_{\rm comm}/k_{\rm B} = 1$.

Suppose the agreement between $-s_{\rm ex,crit}/k_{\rm B} = 1$ and $-s_{\rm comm}/k_{\rm B} = 1$ is not just a coincidence. In that case, our empirical observation might suggest that the centric fluid at the gas-liquid critical point should be thermodynamically equivalent to a system of ideal gas (point-like) particles moving in their cells. It should be stressed that molecules are not actually confined in their cells. Instead, the system entropy should be equally (or similarly) decreased by the repulsive and attractive forces so that the effective volume explored by

a particle is comparable to the cell volume v. In other words, the number of microstates should be reduced, satisfying the following two postulates.

P1 The effective cell size v explored by a molecule should be equal to (or at least comparable to) V/N at the critical temperature; it should be v_{crit} at the gas-liquid critical point.

P2 The effective volume is equally (or similarly) determined by repulsive and attractive interaction; the decrease in the number of microstates by the hard-core (repulsive) interaction and the attractive potential well should be comparable.

To test proposition P1, we need to define the (imaginary) cell size v. Since the second virial coefficient at the critical temperature $B_{2,\mathrm{crit}}$ approximately represents the effective range of interatomic potentials,[29] we see if the magnitude of $B_{2,\mathrm{crit}}$ is similar to v_{crit}.

In the case of the fluids covered in NIST REFPROP, the second virial coefficient at the critical temperature is proportional to the critical volume. The average ratio between $-B_2(T_{\mathrm{crit}})$ and v_{crit} is 1.28±0.12. The heavy noble gases, including argon, krypton, and xenon, show $B_2 \approx -1.15 v_{\mathrm{crit}}$. The comparability between $B_2(T_{\mathrm{crit}})$ and $-v_{\mathrm{crit}}$ can also be illustrated using a truncated virial EOS. When the high-order terms of the virial EOS (B_i where $i \geq 4$) are ignored, the compressibility factor Z is expressed as follows.

$$Z = \frac{p}{\rho k_{\mathrm{B}} T} = 1 + B_2\rho + B_3\rho^2 \tag{4}$$

Using the van der Waals' definition of the gas-liquid critical point, the EOS should satisfy the following condition at the critical density ρ_{crit}.

$$\left(\frac{\partial p}{\partial \rho}\right)_{T_{\mathrm{crit}}} = \left(\frac{\partial^2 p}{\partial \rho^2}\right)_{T_{\mathrm{crit}}} = 0 \tag{5}$$

Inserting Eq. 4 to Eq. 5, we obtain

$$1 + 2B_2\rho_{\mathrm{crit}} + 3B_3\rho_{\mathrm{crit}}^2 = 0 \text{ and} \tag{6}$$

$$3B_3\rho_{\mathrm{crit}} = -B_2, \tag{7}$$

which leads to $B_{2,\mathrm{crit}} = -v_{\mathrm{crit}} = -\rho_{\mathrm{crit}}^{-1}$.

To test proposition P2, we devise an alchemical transformation process to dissect excess entropy based on the Widom insertion formula.[30] In the Widom insertion, the dimensionless

excess chemical potential per particle $\beta\mu_{\mathrm{ex}}$ ($\beta^{-1} \equiv k_{\mathrm{B}}T$) is obtained as

$$\beta\mu_{\mathrm{ex}} = -\ln \mathcal{B}_i = -\ln \langle \exp\left(-\beta\phi_i\right) \rangle \tag{8}$$

where k_{B} is the Boltzmann constant, $\mathcal{B}_i$ is the insertion parameter, and ϕ_i is the interaction energy of an inserted particle i with all preexisting particles in the system. Provided that the particle is perfectly hard (impenetrable), Eq. 8 is transformed into

$$\beta\mu_{\mathrm{ex}} = -\ln P_{\mathrm{ins}} - \ln \langle \exp\left(-\beta\phi_{\mathrm{att,i}}\right) \rangle. \tag{9}$$

where P_{ins} is the probability of inserting a hard-core particle into the system without overlapping preexisting hard-core particles. Two hard-core particles are regarded as overlapped when their distance is shorter than the sum of their radii.

By using the fundamental relation of thermodynamics ($\mu \equiv G/N = (U + pV - TS)/N$) and the definition of excess properties ($\mathcal{P}_{\mathrm{ex}} = \mathcal{P} - \mathcal{P}_{\mathrm{ig}}$), the right-hand side (RHS) of Eq. 9 becomes

$$-\ln P_{\mathrm{ins}} - \ln \langle \exp\left(-\beta\phi_{\mathrm{att,i}}\right) \rangle = \beta u_{\mathrm{ex}} + Z - 1 - s_{\mathrm{ex}}/k_{\mathrm{B}}. \tag{10}$$

where the definition of the compressibility factor $Z = \beta pv$ is introduced. Moving all terms in the RHS of Eq. 10 except $s^{+} = -s_{\mathrm{ex}}/k_{\mathrm{B}}$, we obtain

$$s^{+} = -\ln P_{\mathrm{ins}} - \ln \left(\langle \exp\left(-\beta\phi_{\mathrm{att,i}}\right) \rangle \right) - \beta u_{\mathrm{ex}} + 1 - Z \tag{11}$$

We further dissect each term into repulsive (hard-core) and attractive contributions. First, the insertion term P_{ins} is given as $P_{\mathrm{ins}}^{\mathrm{hs}}(P_{\mathrm{ins}}/P_{\mathrm{ins}}^{\mathrm{hs}})$ where $P_{\mathrm{ins}}^{\mathrm{hs}}$ is the probability of inserting a hard-core particle to the system where no attractive interaction exists. Second, the compressibility factor Z is dissected into Z_{hs} and Z_{att}. Lastly, since no attractive interaction exists in a hard sphere (purely repulsive) system, $u_{\mathrm{ex}} = u_{\mathrm{att}}$. Considering all these relations, the following expression is obtained.

$$s^{+} = \varsigma_{\mathrm{hs}} + \varsigma_{\mathrm{per}} = \varsigma_{\mathrm{hs}} + (\varsigma_{\mathrm{str}} + \varsigma_{\mathrm{energy}}) \tag{12}$$

In Eq. 12, ς_{hs} is the hard-core contribution. The perturbative (attractive) potential contribution ς_{per} is dissected into structural (ς_{str}) and energetic ($\varsigma_{\mathrm{energy}}$) ones. They are given as follows.

$$\varsigma_{\mathrm{hs}} = s_{\mathrm{hs}}^{+} = 1 - \ln P_{\mathrm{ins}}^{\mathrm{hs}} - Z_{\mathrm{hs}} \tag{13}$$

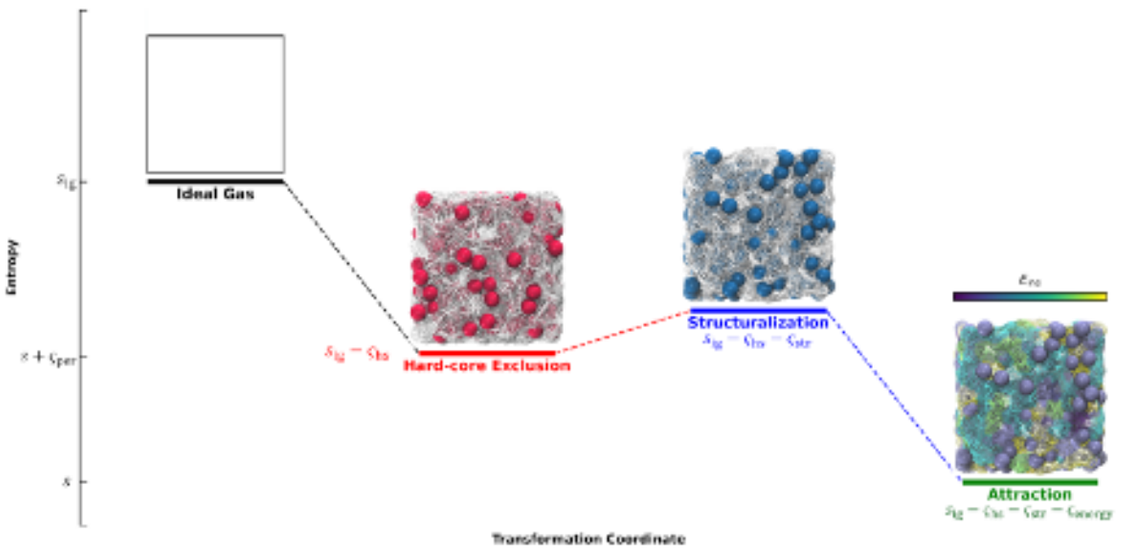

FIG. 2. A schematic diagram of the alchemical transformation to dissect excess entropy into different contributions. This alchemical transformation process consists of three stages. In the first stage (hard-core exclusion), we let N hard spheres (red balls) freely move in the system. The excess entropy of the hard sphere system is a function of the probe-occupiable volume (white mesh) and the hard-sphere compressibility factor. In the second stage (structuralization), we let the hard-core molecules move but turn on the attractive interaction between them. Note that ς_{str} is calculated by averaging all configurations, although only a single configuration is shown in the diagram. The attractive interaction between the preexisting particles results in local cluster(s) formation, which usually increases the probe-occupiable volume. This structural change increases the total entropy ($\varsigma_{\text{str}} < 0$). In the last stage (attraction stage), the entropy decrement due to the local attractive potential (colored mesh) induced by the preexisting particles is considered. This effect is denoted as an energetic term $\varsigma_{\text{energy}}$. The sum of ς_{str} and $\varsigma_{\text{energy}}$ is denoted as ς_{per}.

$$\varsigma_{\text{str}} = -\ln\left(P_{\text{ins}}/P_{\text{ins}}^{\text{hs}}\right) \tag{14}$$

$$\varsigma_{\text{energy}} = -\ln\left\langle \exp\left(-\beta\phi_{\text{att},i}\right)\right\rangle - \beta u_{\text{att}} - Z_{\text{att}} \tag{15}$$

It would be instructive to compare the proposed method to classical perturbation theory. In perturbation theory, an interatomic potential is dissected into the repulsive (hard-core) and perturbative (attractive) parts. Perturbation theory states that the repulsive interaction dominantly determines the structural characteristics of liquids.[7] However, this proposition does not hold in gases and dilute supercritical fluids, as Toxvaerd demonstrated.[31] Since

there is enough space in a dilute system, local clusters are easily formed by the attractive interaction. As a result, $P_{\text{ins}}^{\text{hs}}$ is not equal to P_{ins} in low- to intermediate-density conditions ($\varsigma_{\text{str}} \neq 0$).

In contrast to classical perturbation theory, Eq. 12 does not dissect the interatomic potential between particles. Rather, it dissects the entropic contribution at the system level (Figure 2). In this dissection method, we first consider a system of N ideal gas particles. Since neither repulsion nor attraction exists in the ideal gas system, the system entropy is calculated as given in Eq. 2. The ordering of particles due to the excluded volume effect, also called as *entropic force*,[32] is included by calculating the excess entropy of the hard sphere system; s_{hs}^{+} should be equal to ς_{hs}. Since the hard-core interaction always decreases the probe-available volume in a system, ς_{hs} is positive and approaches zero at the low-density limit ($\rho \to 0$). This hard sphere contribution is calculated using the Carnahan-Starling EOS.[33]

The remaining term ς_{per} is dissected into structural and energetic components ($\varsigma_{\text{per}} = \varsigma_{\text{str}} + \varsigma_{\text{energy}}$). As shown in Eq. 14, the structural term corresponds to the configurational change from a purely repulsive system to a full potential system. Note that ς_{str} is usually negative, which might seem counter-intuitive at first glance. Recall that the local attractive potential pulls hard spheres together, securing a space for a hard-core particle (probe-occupiable volume) to be inserted. As a result, P_{ins} becomes higher than $P_{\text{ins}}^{\text{hs}}$, leading ς_{str} to be negative. At the low-density limit ($\rho \to 0$), ς_{str} converges to zero since particles become too far apart. As ρ increases, its magnitude would increase. However, at the high-density limit ($\rho \to \infty$), it would converge to zero again since particles do not have enough space to move; the solution structure is dominated by the repulsion.

The attractive potential energy term $\varsigma_{\text{energy}}$ denotes the influence of the local attractive interactions between the inserted particle and the preexisting ones. Identical to ς_{str} and ς_{hs}, $\varsigma_{\text{energy}}$ goes to zero as ρ approaches zero. Since the attractive potential is always negative, $\varsigma_{\text{energy}}$ is positive at $\rho > 0$. Note that the sign of ς_{hs} and $\varsigma_{\text{energy}}$ is positive; repulsive and attractive interactions decrease the number of microstates in a system, compared to the ideal gas state. Going back to the similarity between $s^{+} = 1$ and $-S_{\text{comm}}/Nk_{\text{B}} = 1$, we now have a means to test proposition P2; ς_{hs} would be equal or comparable to $\varsigma_{\text{energy}}$ in the centric fluid system if postulate P2 holds.

IV. COMPUTATIONAL DETAILS

A. Model Potentials

We perform a series of molecular simulations of particles interacting via spherically isotropic pair potentials, including the square-well, Lennard-Jones (LJ), Mie n-6, and two-body *ab initio* pair potentials. The square-well potential is one of the simplest models considering attractive and hard-core interactions, which is given as

$$\phi(r) = \begin{cases} \infty & r \leq \sigma \\ -\epsilon & \sigma < r \leq \lambda\sigma \\ 0 & \lambda\sigma < r \end{cases} \tag{16}$$

where λ is the attractive well width parameter. The LJ potential is given as

$$\phi_{\mathrm{LJ}}(r) = 4\epsilon \left[\left(\frac{\sigma}{r}\right)^{12} - \left(\frac{\sigma}{r}\right)^{6} \right] \tag{17}$$

where ϵ and σ are energy and size parameters, respectively. The Mie n–6 potential is given as

$$\phi_{\mathrm{M}}(r) = \left(\frac{n}{n-6}\right) \left(\frac{n}{6}\right)^{6/(n-6)} \epsilon \left[\left(\frac{\sigma}{r}\right)^{n} - \left(\frac{\sigma}{r}\right)^{6} \right] \tag{18}$$

where n is the repulsive exponent. The repulsive exponent (n) in the Mie model is changed from 12 to 14. These values have been used to model the phase behavior of noble gases in earlier works.[34] In all model potentials, we set σ and ϵ to unity ($\sigma = \epsilon = 1.0$). These quantities are dimensionless and used to calculate thermodynamic quantities. For instance, the energy is calculated as $E^* = E/\epsilon$, and force is computed as $f^* = f\sigma/\epsilon$.

The two-body *ab initio* model proposed by Jäger, Hellmann, Bich, and Vogel[35–37] uses the Tang-Toennies potential form to represent the interatomic potential between noble gas molecules. It is given as

$$\begin{aligned} \phi(r) =& A \exp\left(a_1 r + a_2 r^2 + \frac{a_{-1}}{r} + \frac{a_{-2}}{r^2}\right) \\ & - \sum_{n=3}^{8} \frac{C_{2n}}{r^{2n}} \left[1 - \exp\left(-br\right) \sum_{k=0}^{2n} \frac{(br)^k}{k!} \right] \end{aligned} \tag{19}$$

where the dispersion coefficients C_{2n} and the repulsion coefficients A, a_n, and b are obtained by fitting the potential form to the *ab initio* data. For a complete description of Eq. 19, see References 35–37.

When applying the excess entropy dissection method proposed in Sec. III, a hypothetical hard sphere system should be defined for each model. For the square-well system, we use a hard sphere potential with the same hard-core diameter as such a hypothetical one: $\phi_{\rm hs}(r) = \infty$ $(r \le \sigma)$ and $\phi_{\rm hs}(r) = 0$ $(r > \sigma)$. For continuous potential models, we need to define an effective hard-core diameter. Several different methods have been devised to determine the effective hard-core diameter of a continuous potential model based on Rowlinson's concept.[38] We adopt the recent suggestion by Attia, Dyre, and Pedersen.[39] In this method, the hard-core diameter is calculated as the distance where the excess entropy of a soft repulsive particle becomes equal to that of the hard sphere system: $s^+(\mathbf{r}; \phi = \phi_{\rm hs}) = s^+(\mathbf{r}; \phi = \phi_{\rm rep})$.

Following this philosophy, we first define the repulsive portion of the potential based on the suggestion by Weeks, Chandler, and Andersen (WCA).[7] This method defines the repulsive potential $\phi_{\rm rep}(r)$ by shifting and cutting the original potential at its potential minimum $(r = r_{\rm min})$.

$$\phi_{\rm rep}(r) = \begin{cases} \phi(r) - \phi(r_{\rm min}) & r \le r_{\rm min} \\ 0 & r > r_{\rm min} \end{cases} \tag{20}$$

The MD simulation protocol for this purely repulsive system is identical to that of the full potential system, which is written in Sec. IV B. After calculating the excess entropy from the simulation results, the packing fraction of a hard sphere system $(\eta \equiv \pi\rho\sigma_{\rm hs}^3/6)$ that yields the same excess entropy is computed. The hard sphere excess entropy term $(s_{\rm ex,hs})$ is calculated using the Carnahan-Starling EOS,[33] which is given as

$$s_{\rm hs}^+ = -s_{\rm ex,hs} = \frac{\eta(4-3\eta)}{(1-\eta)^2}. \tag{21}$$

The packing fraction making $-s_{\rm ex,hs}$ equal to the excess entropy of the WCA system is found using the Brent's root-finding method. Then, the hard-core diameter $\sigma_{\rm hs}$ is obtained as $\sigma_{\rm hs} = [6\eta/(\rho\pi)]^{1/3}$.

B. Molecular Simulation Details

We use event-driven and time-driven molecular dynamics (EDMD and TDMD) and classical Monte Carlo (MC) simulations to obtain thermodynamic and structural characteristics of the model fluids. DynamO, an open-source event-driven particle simulator,[40] is used to

perform the single-phase EDMD simulations of the hard sphere and square-well fluid systems. Initial configurations containing $N = 2,048$ particles are first generated and relaxed during 10^6 collisions. The particle velocities in the relaxed system are rescaled, and the Andersen thermostat is introduced to reach the specified temperature. The system is thermally equilibrated during 10^7 collisions. Then, the pressure and trajectory data are collected during an additional production run (5×10^7 collisions). The trajectory data are sampled every $50,000$ collisions.

MCCCS Towhee, an open-source Monte Carlo software for molecular simulations,[41] is used to perform the two-phase Monte Carlo (2PMC) simulations of square-well particles for estimating their acentric factors. In the 2PMC simulations, a periodic simulation box whose number density is $\rho^* = \rho\sigma^3 = 0.3$ is first prepared. The number of particles is 2,048. The simulation box lengths (L_x, $L_y\,(= L_x)$, and L_z) are adjusted so that L_x is higher than the particle diameter σ by a factor of ten. The length along the z direction (L_z) is four times longer than L_x.[42] The initial configuration is equilibrated during 1,000,000 steps (10^9 moves). Then, the system configurations are collected every $10,000$ steps during the production run ($5,000,000$ steps).

Large-scale Atomic/Molecular Massively Parallel Simulator (LAMMPS, 23 Jun 2022)[43] is used to perform the TDMD simulations of the noble gases modeled with the LJ, Mie n–6, and two-body *ab initio* potentials. The LJ and Mie n–6 potentials are already implemented in LAMMPS, but the *ab initio* potential is not. Thus, a tabulated form of the *ab initio* potential is constructed from $r = 0.2$ Å to $r = 14$ Å with an interval of $\Delta r = 0.01$ Å, based on an earlier work.[13] In all single-phase simulations, the particles are randomly placed in a simulation box with arbitrary velocities. The system is equilibrated for 5 ns. Then, the pressure and trajectory data are collected every 5 ps during the production run (10 ns). The timestep is 1 fs. In two-phase (2PMD) simulations, the number of molecules and the simulation box dimensions are the same as those of the 2PMC simulations.

C. Estimation of the Gas-Liquid Critical Point

Although the pair potentials used in this work have been extensively studied, their critical properties and acentric factors ($T_{\rm crit}$, $p_{\rm crit}$, $\rho_{\rm crit}$, and ω) from earlier works are scattered, depending on the methodology and simulation details.[44–51] For consistency, we re-estimate

their critical properties based on van der Waals' definition of the gas-liquid critical point.[52] As shown in Eq. 5, the first and second derivatives of the pressure with respect to the density should be zero at the gas-liquid critical point. By regressing a cubic polynomial ($p = a\rho^3 + b\rho^2 + c\rho + d$) to the pressure data obtained along different isotherms, we first determine inflection densities at different temperatures ($\rho_{\text{inf}} = -b/3a$). Then, T_{crit} is computed as where the slope at the inflection density ($dp/d\rho$ at $\rho = \rho_{\text{inf}}$) becomes zero. The critical density (ρ_{crit}) is calculated as the inflection density (ρ_{inf}) at $T = T_{\text{crit}}$. The critical pressure (p_{crit}) is calculated by interpolating the pressure-density curve along the critical isotherm. For a detailed calculation protocol and comparison between the obtained data and literature, see Sec. S2 in Supplementary Material.

D. Estimation of the Acentric Factor

After estimating T_{crit}, the saturation densities (ρ_{gas} and ρ_{liq}) are calculated at $T_{\text{r}} = 0.7$ by performing the 2PMD/2PMC simulations. In this method, the trajectory data are used to construct a histogram of the particle density along the z direction. This profile is fitted to a sigmoid function (Eq. 22) by applying the Levenberg-Marquardt algorithm.[42]

$$\rho(z) = \frac{1}{2}(\rho_{\text{liq}} + \rho_{\text{gas}}) - \frac{1}{2}(\rho_{\text{liq}} - \rho_{\text{gas}}) \tanh\left[\frac{\theta(z - z_0)}{\delta}\right] \tag{22}$$

In Eq. 22, ρ_{liq} and ρ_{gas} are saturation liquid and vapor densities, respectively. The regression parameters (ρ_{gas}, ρ_{liq}, δ, θ, and z_0) are initially set to be one. After estimating ρ_{gas} and ρ_{liq}, NVT simulations are performed at $T_{\text{r}} = 0.7$ and $\rho = \rho_{\text{gas}}$ to obtain the saturation pressure.

The uncertainties of acentric factors are estimated as follows. After estimating the uncertainties of the critical temperature (δT_{crit}) as described in Sec. IV C, three independent simulations at different temperatures ($0.7(T_{\text{crit}} + \delta T_{\text{crit}})$, $0.7T_{\text{crit}}$, and $0.7(T_{\text{crit}} - \delta T_{\text{crit}})$) are performed to calculate the saturation densities. Then, the averages and uncertainties of the saturation pressure data along three different isotherms are calculated. For the detailed results, see Sec. S3 in Supplementary Material.

E. Calculation of the Excess Entropy

We implement the excess entropy dissection method in Sec. III by combining two algorithms proposed by Sastry et al.[53] and Bieshaar et al.[54], which were constructed based on

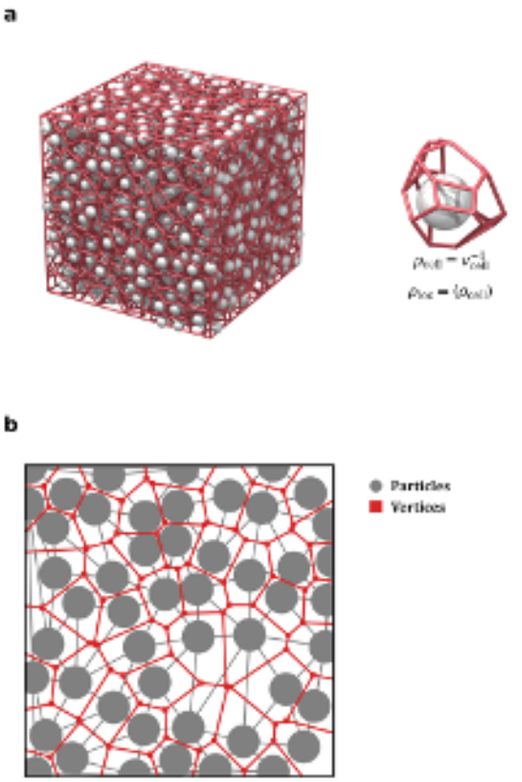

FIG. 3. **a** An illustration of the three-dimensional Voronoi tessellation. In Voronoi tessellation, a system of consist of N particles is dissected into N Voronoi cells. Each cell contains a single particle enveloped by planes perpendicularly bisecting the line connecting a central atom and its neighbors. The shape and size of the Voronoi cell contain fruitful information about its local environment. For instance, the local density of a molecule is defined as $\rho_{\text{cell}} = 1/v_{\text{cell}}$ where v_{cell} is the cell volume. **b** A two-dimensional representation of the Voronoi-Delaunay tessellation. In this method, voids are detected using the Voronoi vertices (red squares). Then, the Delaunay simplices enveloping the voids (triangles connecting gray atoms) are used to calculate the void volume.

Voronoi tessellation. In Voronoi tessellation, a space consisting of N particles is partitioned into N cells. The Voronoi cell consists of all points closer to the seed particle (central particle) than the other particles. (Figure 3a) Since the Voronoi cell contains abundant information about the interaction between a central particle and its neighbors, this technique has been utilized as a computational tool to characterize the structural characteristics of particle systems.[55]

Sastry et al. employed the Voronoi-Delaunay tessellation technique to calculate the probe-occupiable volume in the system configuration generated from molecular simulations.[53] This algorithm detects a void using the Voronoi vertices and edges (Figure 3b). Then, the polyhedron enclosing the cavity is identified and dissected into subsimplices. The cavity volume is calculated by summing up the subsimplices' volumes. Compared to conventional MC algorithms, this algorithm greatly reduces the statistical uncertainty in estimating the probe-occupiable space. We calculate ς_{hs} and ς_{str} via the Sastry method.

Bieshaar et al.,[54] independent from Sastry et al., proposed an algorithm to perform the Widom insertion in high-density systems. In this method, a probe particle is inserted into the grid constructed near the Voronoi vertices. Since these Voronoi vertices are probably most distant from all neighbors (Figure 3b), a particle inserted into the grid points has a lower chance of overlapping with preexisting particles. This insertion algorithm reduces the number of trials required for calculating the excess chemical potential in a high-density system, improving the calculation accuracy of $\varsigma_{\mathrm{energy}}$.

To ensure the robustness of the Sastry-Bieshaar method, we compare the calculated s^+ data to those obtained using the Deiters-Hoheisel method. In the Deiters-Hoheisel method,[56] the dimensionless excess chemical potential $\beta\mu_{\mathrm{ex}}$ is calculated as

$$\beta\mu_{\mathrm{ex}} = \int_0^{\rho} \frac{Z-1}{\rho} d\rho + Z - 1 \tag{23}$$

where Z is the compressibility factor ($Z \equiv p/\rho k_{\mathrm{B}}T$), and ρ is the number density. The integrand $(Z-1)/\rho$ term converges to the second virial coefficient B_2 at the low-density limit.[13] The integral term in Eq. 23 is calculated by constructing a spline function in the density region between 0 and ρ. Then, s^+ is computed using the fundamental relation of thermodynamics.[12]

The average absolute relative deviation (AARD) between the two methods is 0.3 %. See Sec. S4 in Supplementary Material for the detailed analysis of the deviation between the two methods.

F. Structural Analysis

In addition to thermodynamic characteristics, we examine the structural features, including the radial distribution function ($g(r)$), multi-particle excess entropy ($s_{\mathrm{M,ex}}$), and local

density augmentation ($\Delta\rho_{\rm loc}$). The radial distribution function $g(r)$, one of the most useful measures of the fluid structure, shows how the coordination structure is formed as a result of the complex interaction inside the system. It is also directly related to the two-body excess entropy ($s_{2,\rm ex}$), which is given as:

$$s_2^+ = -\frac{s_{2,\rm ex}}{k_{\rm B}} = 2\pi\rho \int_0^\infty [g(r)\ln g(r) - g(r) + 1]r^2 dr \tag{24}$$

The two-body excess entropy has been widely used as a good approximation to the excess entropy in low-density (gas-like) systems. However, the many-body contribution to forming the coordination structure becomes important in high-density systems. This many-body contribution, also called as the multi-particle excess entropy ($s_{\rm M,ex} \equiv -k_{\rm B}s_{\rm M}^+ = s_{\rm ex} - s_{\rm ex,2}$), has been used as another sensitive measure to examine the structural transition in a fluid system.[57,58] We calculate $s_{\rm M}^+$ to understand how an interatomic potential affects the multi-particle contribution to forming the coordination structure.

In near-critical fluids, the local density of solvents near a solute is greater than the bulk solvent density.[59–66] The difference between the average local density of a molecule ($\langle\rho_{\rm loc}\rangle$) and the bulk (system) density (ρ) is defined as the local density augmentation: $\Delta\rho_{\rm loc} \equiv \langle\rho_{\rm loc}\rangle - \rho$. The maximum local density augmentation is usually observed at $\rho < \rho_{\rm crit}$ (not at $\rho = \rho_{\rm crit}$), which was one of the riddles in supercritical fluid science and technology. Maddox, Goodyear, and Tucker suggested that the local density is most augmented below the critical density as a result of the competition between the critical density fluctuation and the potential-induced effect.[61] However, they did not quantitatively examine how the interplay between the local potential-induced effect and the critical density fluctuation determines where $\Delta\rho_{\rm loc}$ is maximized.

To calculate the local density augmentation, we again adopt the Voronoi tessellation to define the local density of an individual atom.[59,60] The VORO++ software developed by Rycroft[55] is used to dissect the system into Voronoi cells. Then, the local density of a molecule is computed as the reciprocal of the Voronoi cell volume $v_{\rm cell}$. ($\rho_{\rm cell} = 1/v_{\rm cell}$) The arithmetic mean of the local density data of all molecules is defined as the mean local density.

$$\langle\rho_{\rm loc}\rangle = \frac{1}{N}\sum_{i=1}^{N}\rho_{{\rm cell},i} \tag{25}$$

Note that $\langle\rho_{\rm loc}\rangle$ is equal to the bulk density ρ only when the arithmetic mean of the local density is the same as the harmonic mean. Since molecules attract each other, either by

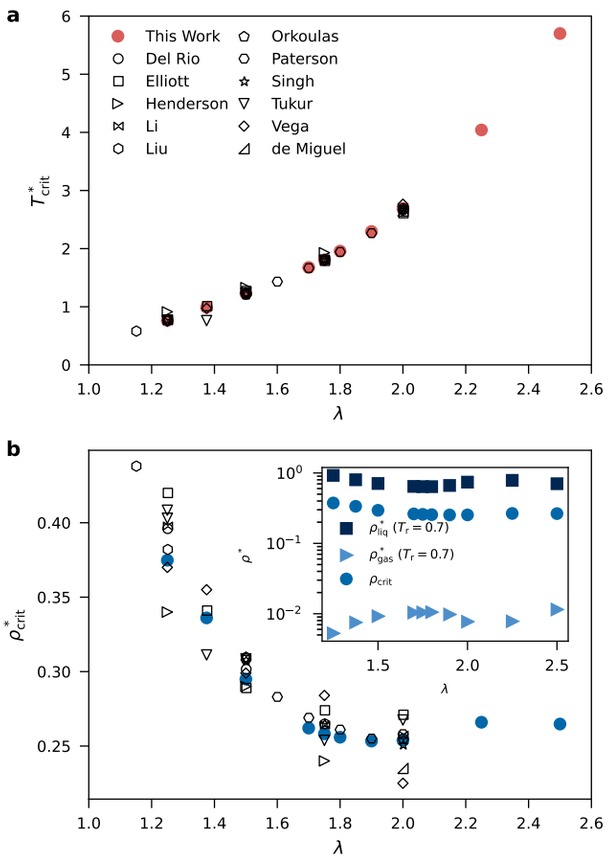

FIG. 4. **a** Dimensionless critical temperature ($T^*_{\text{crit}} \equiv k_{\text{B}}T_{\text{crit}}/\epsilon$) and **b** dimensionless critical density $\rho^*_{\text{crit}} \equiv \rho\sigma^3$ and vapor-liquid coexistence densities (ρ^*_{gas} and ρ^*_{liq}, the inset graph) as a function of the well width λ. As λ increases, T^*_{crit} monotonically increases, while ρ^*_{crit}, ρ^*_{liq}, and ρ^*_{gas} show extrema near $\lambda = 1.8$. This oscillatory behavior signifies the effect of acentricity on the thermophysical properties of fluid systems.

repulsion (hard-sphere exclusion) or attraction (local cluster formation), the (arithmetic) mean local density is usually higher than the bulk density.

V. RESULTS AND DISCUSSIONS

A. Square-well Simulations

Figure 4 shows the dimensionless critical temperature ($T^*_{\text{crit}} \equiv k_{\text{B}}T_{\text{crit}}/\epsilon$) and density ($\rho^*_{\text{crit}} \equiv \rho_{\text{crit}}\sigma^3$) as a function of the attractive well width λ (See Sec. S5 of Supplementary

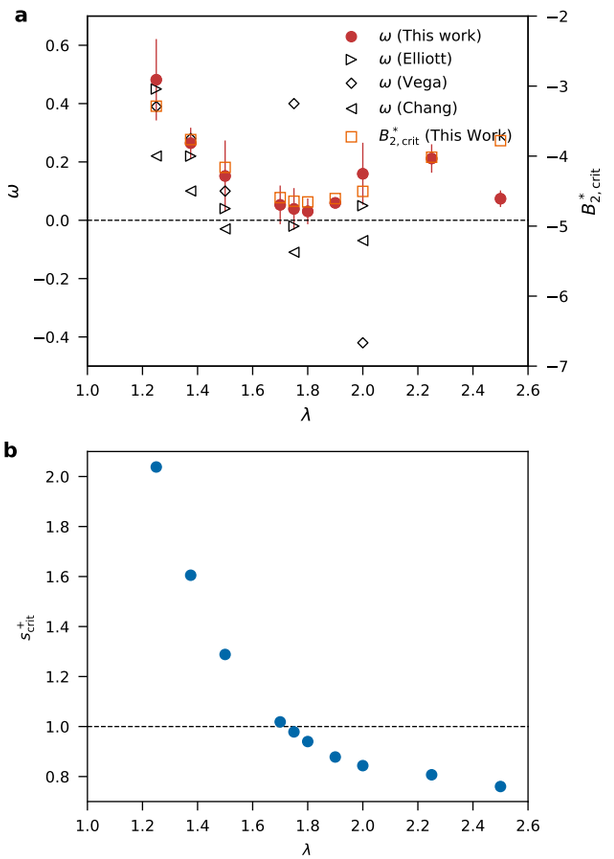

FIG. 5. **a** Acentric factors (ω) and dimensionless second virial coefficients ($B^*_{2,\mathrm{crit}} \equiv B_{2,\mathrm{crit}}/\sigma^3$) as a function of the attractive well width (λ). The acentric factor of a square-well model becomes closest to zero near $\lambda = 1.8$ where the coexistence densities show extrema. The $B^*_{2,\mathrm{crit}}$ values also show a minimum at the same well width. **b** The s^+_{crit} values of square-well model fluids with different well widths. Unlike Pitzer's expectations,[19] s^+_{crit} does not show a minimum when the particle becomes most centric ($\lambda = 1.8$). Instead, s^+_{crit} monotonically decreases as the attractive well width increases.

Material for numerical data). As λ increases, T^*_{crit} monotonically increases, whereas ρ^*_{crit} shows an oscillatory behavior, which was also noted by Reyes et al.[67] The vapor-liquid coexistence densities (ρ^*_{gas} and ρ^*_{liq} at $T_{\mathrm{r}} = 0.7$) also show extrema at $\lambda = 1.8$.

Figure 5a shows that the dimensionless second virial coefficient at the critical temperature $B^*_{2,\mathrm{crit}}(\equiv B_{2,\mathrm{crit}}/\sigma^3)$ and the acentric factor ω also have their minima at $\lambda = 1.8$. Note that the ω minimum is closest to zero; the fluid becomes most centric at $\lambda \approx 1.8$. The average $-B_{2,\mathrm{crit}}$ to v_{crit} ratio is calculated as 1.17 ± 0.08; proposition P1 approximately holds in all

square-well fluids. For the detailed numerical data, see Table S5 in Supplementary Material.

The oscillatory dependence of ω on the attractive well width λ indicates that the spherical symmetry (hypothesis H2) is insufficient to regard a molecule as *centric*. Instead, the nature of interatomic potential plays a critical role in determining ω, as hypothesis H5 proposes. While ω shows a complex dependence on λ, $s^+_{\rm crit}$ monotonically decreases as λ increases (Figure 5b). Note that the excess entropy is not lowest in the centric fluid system unlike Pitzer's expectations.[19] The wider the attractive well width is, the lower the $s^+_{\rm crit}$ values are. The $s^+_{\rm crit}$ value becomes close to unity at $\lambda = 1.8$ and can be used to identify how the narrowness of an attractive well affects thermodynamic properties. All these results propose that the empirical link between $s^+_{\rm crit} \approx 1$ and $\omega \approx 0$ is valid in square-well systems.

Figure 6 demonstrates how each entropic contribution ($\varsigma_{\rm hs}$, $\varsigma_{\rm str}$, and $\varsigma_{\rm energy}$) evolves as the system density changes. For the other square-well systems, see Sec. S6. As ρ^* increases, $\varsigma_{\rm hs}$ monotonically increases, whereas $\varsigma_{\rm per}$ shows a maximum below $\rho_{\rm crit}$ ($0.9 < \rho_{\rm r} < 1.0$) regardless of the square-well width λ, which reminds us of the local density enhancement observed in earlier works.[59,61,62,64] That is, the behavior of $\varsigma_{\rm per}$ is independent from the (a)centricity. On the other hand, $\varsigma_{\rm str}$ and $\varsigma_{\rm energy}$ show a complex dependence on λ (or ω) and ρ. When λ is low, $\varsigma_{\rm energy}$ and $\varsigma_{\rm str}$ reach their extrema at $\rho > \rho_{\rm crit}$. As λ becomes close to 1.8, the densities where both properties reach their extrema become close to $\rho_{\rm crit}$. At $\lambda > 1.8$, $\varsigma_{\rm energy}$ and $\varsigma_{\rm str}$ become close to zero and reach their extrema at $\rho > \rho_{\rm crit}$ again. In addition, $\varsigma_{\rm energy}$ at $\rho \approx \rho_{\rm crit}$ becomes smaller than $\varsigma_{\rm hs}$ in the square-well fluids with $\lambda > 1.8$.

Figs. 7a and b demonstrates the similarity between $\varsigma_{\rm per}$ and the local density augmentation ($\Delta\rho_{\rm loc}$). In all square-well fluids, the magnitude of $\Delta\rho_{\rm loc}/\rho_{\rm crit}$ reaches its maximum at the characteristic densities where $\varsigma_{\rm per}$ peaks. Following the idea of Maddox et al.,[61] this result enables us to quantitatively interpret the competition between the local attractive potential and the critical long-length-scale density fluctuation from an excess entropy point of view; $\varsigma_{\rm str}$ is directly related to the critical density fluctuation, while the $\varsigma_{\rm energy}$ term corresponds to the coordination structure formation inside the attractive well. At low density, increasing the system density increases the number of particles within the attractive well. The local structuring of atoms inside the attractive well decreases the local entropy ($\varsigma_{\rm energy} > 0$). Simultaneously, clustering of particles inside the well secures enough space for a particle to be inserted. As a result, $\varsigma_{\rm str}$ decreases ($\varsigma_{\rm str} < 0$). As the density increases further, no more particles can enter the attractive well, which manifests as a reduction in the magnitude of

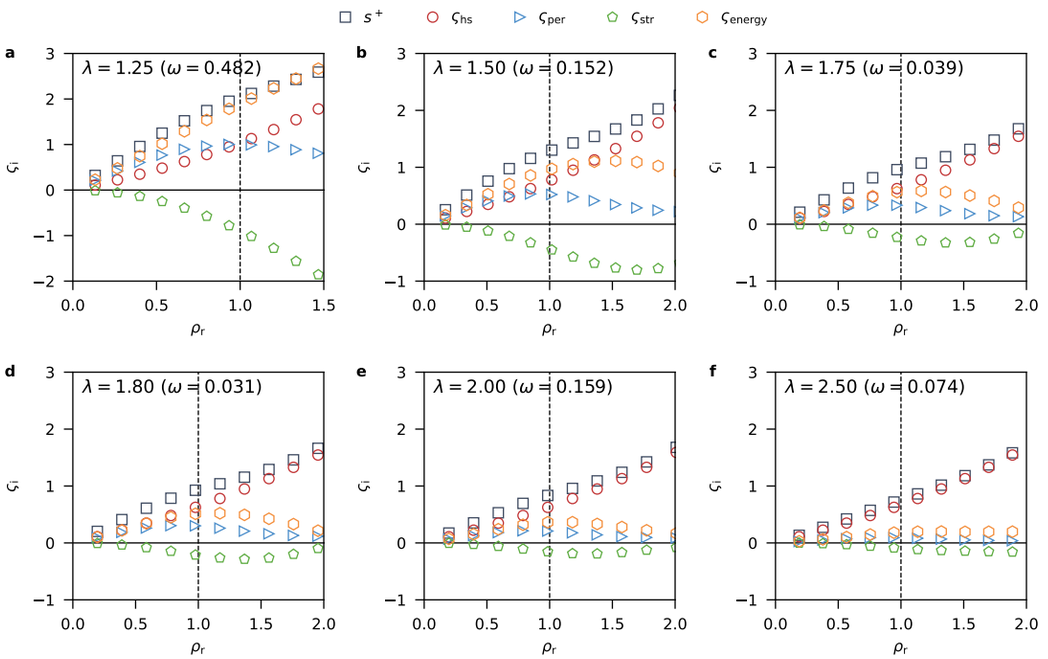

FIG. 6. The density dependence of dimensionless excess entropy ($s^+ \equiv -s_{ex}/k_B$) and its components (ς_{hs}, ς_{str}, and ς_{energy}) of the square-well fluids along the critical isotherm ($T = T_{crit}$): **a** $\lambda = 1.25$ ($\omega = 0.482$), **b** $\lambda = 1.50$ ($\omega = 0.152$), **c** $\lambda = 1.75$ ($\omega = 0.039$), **d** $\lambda = 2.0$ ($\omega = 0.159$), **e** $\lambda = 2.25$ ($\omega = 0.212$), and **f** $\lambda = 2.50$ ($\omega = 0.074$). The ς_{per} value reaches its maximum below the critical density, which results from the combination of the system-wide critical density fluctuation and local attractive interactions. When a fluid becomes most centric ($\lambda \approx 1.80$), ς_{hs} and ς_{energy} become comparable below $\rho = \rho_{crit}$ (vertical dashed lines), supporting our hypothesis P2. In addition, the densities where ς_{str} and ς_{energy} reach their own extrema become closest to the critical density when ω becomes closest to zero.

both ς_{str} and ς_{energy}.

Apart from this centricity-independent behavior, we also observe the centricity dependency of entropic characteristics. When λ is lower than 1.7, ς_{energy} is higher than ς_{hs} at low densities ($\rho < \rho_{crit}$). They become comparable ($\varsigma_{energy} \approx \varsigma_{hs}$) in the nearly centric fluids ($\lambda \approx 1.8$ and $\omega \approx 0$, Fig. 6**c** and **d**). In high-λ fluids, ς_{energy} is always lower than ς_{hs}. Considering that all model fluids are simulated along their critical isotherms, the comparability between ς_{hs} and ς_{energy} observed at $\lambda \approx 1.8$ is not related to the critical density fluctuation but to the model potential's intrinsic nature. Together with postulate P1, this result elu-

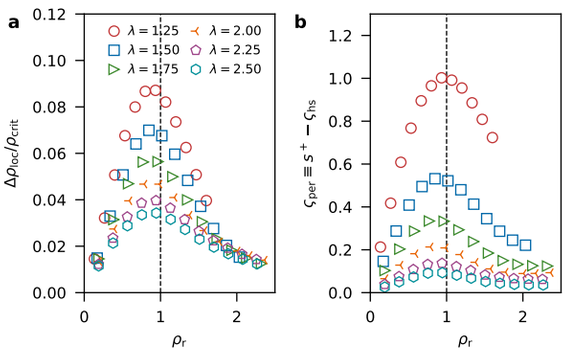

FIG. 7. The density dependence of **a** the normalized local density augmentation ($\Delta\rho_{\mathrm{loc}}/\rho_{\mathrm{crit}}$) and **b** the negative of dimensionless perturbative (attractive) excess entropy contributions (ς_{per}) along the critical isotherm ($T = T_{\mathrm{crit}}$). Regardless of the square-well width (λ), Both properties show their own maxima at the same densities. This result suggests that the characteristic density where the ς_{per} value becomes maximum is determined by the system-wide structuring (both critical density fluctuations and hard sphere contributions) and local attractive interactions.

cidates the mechanism of $s^{+}_{\mathrm{crit}} \approx 1$ and gives a physical ground for hypothesis H5 proposed by Pitzer. At the gas-liquid critical point of centric fluids, the hard sphere and (attractive) energetic contributions to the total excess entropy become comparable in a centric fluid, which makes the particle behave like an ideal gas confined in its (imaginary) cell from an entropic point of view.

Recalling that both ς_{hs} and $\varsigma_{\mathrm{energy}}$ terms contribute to the formation of coordination structures in a fluid system, we analyze the structural characteristics in terms of the radial distribution function $g(r)$. Figure 8a shows how the hard sphere exclusion term contributes to the coordination structure formation. As the system density increases, the oscillatory behavior of $g(r)$ becomes apparent. This oscillatory behavior is a signature of the system-wide structuring driven by the hard-core (volume) exclusion. In the followings, we will use the distances where $g(r)$ reaches its local minima as the first (FCS) and the second coordination shell (SCS) (not where $g(r)$ becomes discontinuous).

Figure 8b–d shows how the attractive interaction perturbs the coordination structure formed by the hard-core exclusion ($\lambda = 1.25$, 1.75, and 2.5). For the other square-well fluids, see Sec. S9 in Supplementary Material. When λ is 1.25, no local minimum is observed within the attractive well, indicating that the short-range attractive interaction, in fact, *hampers*

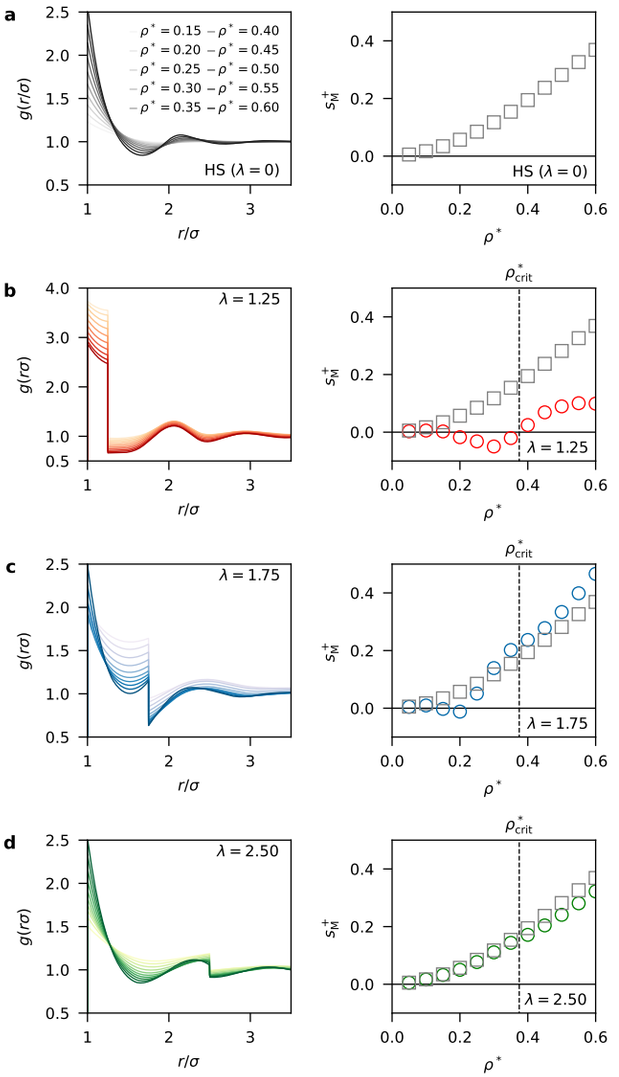

FIG. 8. Radial distribution functions ($g(r)$, left) and negative dimensionless multi-particle excess entropy (s_{M}^{+}, right) data of discrete potential models along the critical isotherm ($T = T_{\mathrm{crit}}$): **a** hard sphere, **b** $\lambda = 1.25$, **c** $\lambda = 1.75$, and **d** $\lambda = 2.50$ square-well fluids. In the hard sphere fluid model, the oscillation of $g(r)$ is observed without a discontinuity, which demonstrates the formation of the first and second coordination shells. In the acentric fluids ($\lambda = 1.25$ and $\lambda = 2.5$), the attractive interaction *hampers* the FCS and SCS formation, which manifests as a discontinuity in $g(r)$ and s_{M}^{+} values lower than those of the hard sphere system. The s_{M}^{+} values suggest that the coordination shells are most structured in the near-centric ($\lambda = 1.75$) fluid.

the FCS formation; the solution structure is dominated by the local attractive potential ($\varsigma_{\rm energy} > \varsigma_{\rm hs}$). On the contrary, in $\lambda \geq 1.70$ fluids, $g(r)$ shows a local minimum within the attractive well; the system-wide structuring induced by the hard-core exclusion is able to form the FCS. In the high-λ fluids ($\lambda > 2$), the FCS is well formulated without the interference of the attractive well, but $g(r)$ becomes discontinuous at the distance where the SCS is formed; the attractive interaction suppresses the SCS formation. This result explains why the $\varsigma_{\rm str}$ and $\varsigma_{\rm energy}$ terms do not vanish even at high densities, although their magnitudes are small. Reyes et al.[67] interpreted the qualitative change of $g(r)$ within $r = \lambda$ in terms of the *saturation* inside the attractive well. On the other hand, the comparability between $\varsigma_{\rm hs}$ and $\varsigma_{\rm energy}$ makes us interpret the qualitative change in FCS and SCS as a competition between the energy-driven (attractive) clustering and the system-wide (hard sphere driven) structuring.

The competition between the hard sphere and local attractive contributions may reduce or strengthen the multi-particle contribution to the formation of coordination shells. The right column of Figure 8 compares the multi-particle term $s_{\rm M}^{+} \equiv -s_{\rm ex,M}/k_{\rm B}$ of the hard sphere and those of square-well fluids. The multi-particle terms of the $\lambda < 1.9$ fluids are almost zero at low densities ($\rho^* < \rho^*_{\rm crit}$) and become close to that of the hard sphere fluid in the low-density region of high-λ fluids ($\lambda \geq 2$). That is, at low densities, the formation of small clusters driven by the attractive interaction reduces $|s_{\rm M}^{+}|$, supporting our observation that the attractive interaction prevents the hard sphere driven ordering.

At $\rho^* > \rho^*_{\rm crit}$, only do the $s_{\rm M}^{+}$ values of the most centric fluid ($1.7 \leq \lambda \leq 1.9$) become higher than that of the hard sphere fluid. This result demonstrates that the high-density centric fluid is most structured with the aid of both hard sphere and attractive potential contributions, as inferred from the $g(r)$ data; they do not interrupt each other. This harmonization also helps us understand why the vapor-liquid density gap width and the critical density become minimum in the centric fluid; the lowest number of particles are required to form liquid-like clusters.

B. Testing the Link for Continuous Potentials

We continue to test the link between $s_{\rm crit}^{+} = 1$ and $\omega = 0$ in continuous potential models (Lennard-Jones, Mie n-6, and two-body *ab initio* potentials). The critical point ($T_{\rm crit}$, $\rho_{\rm crit}$,

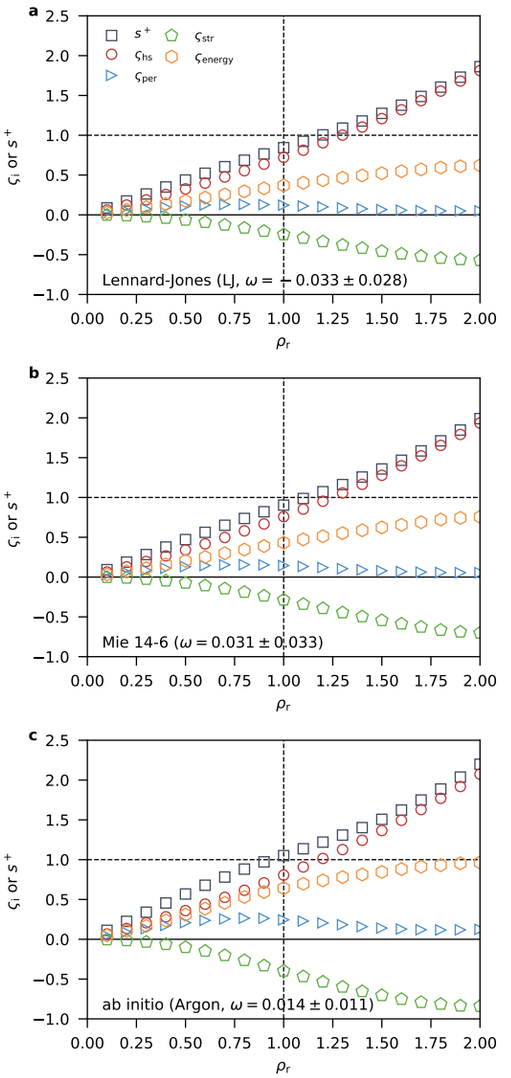

FIG. 9. The s^+ dissection results of the **a** Lennard-Jones (LJ), **b** Mie 14-6, and **c** two-body *ab initio* argon models along the critical isotherm ($T = T_{\text{crit}}$). The s^+_{crit} calculated using the two-body *ab initio* model is closest to unity. As observed in the square-well model systems, ς_{hs} becomes comparable to $\varsigma_{\text{energy}}$ in the two-body *ab initio* model, which is most centric ($\omega \approx 0$ and $s^+_{\text{crit}} \approx 1$). This result again demonstrates that hypothesis P2 would hold in centric fluid systems.

and p_{crit}) estimated based on the van der Waals method are given in Sec. S7 of Supplementary Material. They show a reasonable agreement with earlier works.[68–70] The $-B_{2,\text{crit}}$ to v_{crit} ratio, which can be found in Tables S6 and S7 of Supplementary Material, becomes closest to the NIST REFPROP results ($-B_{2,\text{crit}}/v_{\text{crit}} \approx 1.15$) in the noble gases modeled with the two-

body *ab initio* potential. In Lennard-Jones and Mie n-6 models, the ratios are approximately 0.99. Hence, proposition P1 approximately holds in all continuous models.

Figure 9 shows how the ς_{hs}, ς_{str}, and $\varsigma_{\text{energy}}$ terms evolve in LJ, Mie 14-6, and two-body *ab initio* (argon) models. For the other model potentials, see Sec. S8 in Supplementary Material. Similar to the results obtained in the most centric square-well fluid ($\lambda = 1.80$), s^+_{crit} becomes approximately unity in the two-body *ab initio* argon, krypton, and xenon. It is below unity in the LJ ($s^+_{\text{crit}} = 0.844$ ($n = 12$)) and Mie n-6 fluids ($s^+_{\text{crit}} = 0.876$ ($n = 13$) and 0.903 ($n = 14$)). Moreover, akin to the most centric square-well fluid ($\lambda = 1.8$), ς_{hs} and $\varsigma_{\text{energy}}$ are comparable up to the critical density in the two-body *ab initio* model fluids. In the LJ and Mie n–6 potentials, ς_{hs} is always higher than $\varsigma_{\text{energy}}$. The only difference between the two-body *ab initio* potential and the $\lambda = 1.8$ fluid is the behavior of ς_{str} and $\varsigma_{\text{energy}}$ at high densities, which would come from the softness of the repulsive part, allowing the particles to rearrange more freely.

Figure 10a shows that the link between $s^+_{\text{crit}} = 1$ and $\omega = 0$ is still valid in the two-body *ab initio* model fluids ($\bar{\omega} = 0.014$). They are located near the empirical correlation suggested in Sec. II. Interestingly, the acentric factor of the LJ potential, which is most widely used to model (pseudo)atoms in the field of molecular simulations, is farthest from the centricity ($\omega = -0.033$), which is close to that obtained from the ancillary equations proposed by Thol et al. ($\omega = -0.043$).[71] Instead of the empirical relation obtained from the NIST REFPROP database, an independent linear relationship between s^+_{crit} and ω is observed in the Mie n-6 models ($12 \leq n \leq 14$), revealing the non-correctable bias of the generic n–m potentials[72,73] in representing the entropy-related properties.

Figure 10b compares LJ, Mie n-6, and two-body *ab initio* potentials. As the interatomic distance increases, the repulsive part of all Mie n-6 models ($n \geq 12$) decreases more steeply than that of the two-body *ab initio* model does, suggesting that the effective hard sphere diameter of Mie n-6 fluids explored in this work should be larger than that of the two-body *ab initio* model. As a result, ς_{hs} dominates the entropy decrease of the system, resulting in $\varsigma_{\text{hs}} > \varsigma_{\text{energy}}$ in all thermodynamic conditions. The bias induced by the imbalance between repulsive and attractive forces in the LJ and Mie fluids is also apparent when comparing the second virial coefficients at the critical temperature ($B_{2,\text{crit}}$)[13] and the NIST REFPROP database. The $|B_{2,\text{crit}}|$ values of the *ab initio* potential, which can be found in Tables S6 and S7 of Supplementary Material, are always higher than those of the Mie n-6 models and

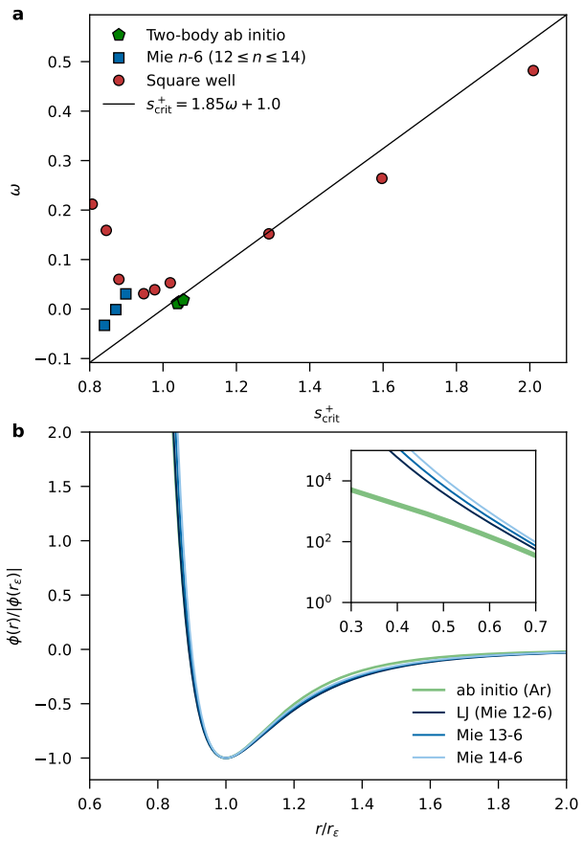

FIG. 10. **a** Relationship between s^+_{crit} and ω in different model fluids. In the two-body *ab initio* model, s^+_{crit} is close to unity at $\omega = 0$, satisfying our empirical observation (solid line). On the other hand, Mie n-6 models form an independent linear relaionship between s^+_{crit} and ω. Square-well fluids show ω minimum near the empirical model. **b** Comparison of interatomic potentials (two-body *ab initio* and Mie n-6 models). While the attractive tails of the Mie n-6 models are slightly heavier than the two-body *ab initio* model, their repulsive parts (see inset) are much steeper than that of the two-body *ab initio* model.

are closest to the experimental result, which again supports our insights obtained from the square-well simulation results: the minimization of $B_{2,\text{crit}}$ in the centric fluid system.

Since the attractive well is smooth in continuous potential models, it is difficult to directly examine the difference by observing how $g(r)$ evolves. Instead, s^+_{M} can be used to examine how the coordination structure is formed. (Figure 11a and b) The dependence of s^+_{M} on the bulk density suggests that the more centric a particle is, the higher the s^+_{M} values are at high densities. Hence, the centric fluids are again proven to be the most structured as a

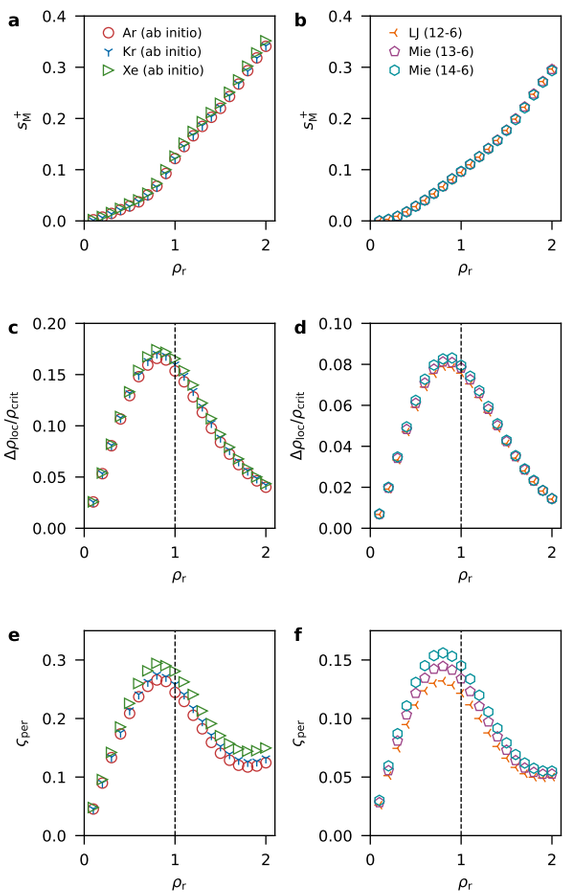

FIG. 11. Structural characteristics of the two-body *ab initio*, LJ, and Mie n-6 potentials along the critical isotherm ($T = T_{crit}$): $s_M^+ = -s_{M,ex}/k_B$ (**a** and **b**), $\Delta\rho_{loc}/\rho_{crit}$ (**c** and **d**), and ς_{per} (**e** and **f**). As shown in **a** and **b**, the s_M^+ values of the two-body *ab initio* model are higher than the other models at high densities, signifying the structurability of centric fluids ($\omega \approx 0$). Regardless of the acentric factor, the characteristic density where $\Delta\rho_{loc}/\rho_{crit}$ becomes maximum (**c** and **d**) aligns well with where ς_{per} becomes maximum (**e** and **f**). These results agree with our observations obtained in square-well systems.

consequence of the hard sphere (volume exclusion) and local potential-induced effects, which are comparable to each other from an entropic point of view.

Lastly, we examine if the centricity-independent structural feature is reproducible in the continuous potential models. Figure 11c–f demonstrates that the characteristic density where ς_{per} shows its maximum aligns well with where the local density augmentation occurs. Moreover, similar to the square-well systems, the characteristic density where ς_{per} and

$\Delta\rho_{\rm loc}/\rho_{\rm crit}$ reach their maxima becomes closest to the critical density in the two-body *ab initio* system, which fulfills the link between $s_{\rm ex,crit} \approx -k_{\rm B}$ and $\omega \approx 0$.

VI. CONCLUSIONS

This work reveals a tight connection between the excess entropy ($s_{\rm ex}$) at the gas-liquid criticality and the acentric factor (ω), a conceptual number introduced by Pitzer to quantify a molecule's nature to deviate from the corresponding state principle. By reviewing the hypotheses proposed by Pitzer to define the centric fluid ($\omega = 0$), we attempt to find a physical basis for his last hypothesis about the necessary condition of the interatomic potential for a molecule (particle) to be *centric*.

Starting from an empirical observation, we discover that $s_{\rm ex,crit}$ approximates $-k_{\rm B}$ in centric fluids ($\omega = 0$). Based on classical cell theory, we postulate that this equality might mean that the repulsive and attractive contributions to the excess entropy are comparable at the gas-liquid critical point of a centric fluid, which leads the system to behave like a confined ideal gas system from a thermodynamic point of view. In order to validate this idea, we scrutinize two propositions. We first validate that the effective volume explored by a molecule at the gas-liquid criticality, which approximates the second virial coefficient, is close to the critical volume. Specifically, the ratio between the second virial coefficient at the gas-liquid critical temperature and the critical volume is obtained as 1.15 in noble gases, which are regarded to be most centric.

Second, we apply an alchemical transformation method to dissect excess entropy into hard-core, structural, and energetic contributions. In both discrete and continuous potential models, we observe both centricity-independent and dependent behaviors. Regardless of the acentric factor, the perturbative (attractive) contribution, which is a sum of the structural and energetic contributions, is maximized at where the local density is most augmented. This result demonstrates the competition between the system-wide critical fluctuation and the local potential energy to determine the solution structure. In addition, we observe that the repulsive (hard-core) contribution to the excess entropy becomes comparable to the energetic contribution when a fluid is centric. In square-well models, the fluid whose well width is approximately 1.8 is most centric. In continuous potential models, the two-body *ab initio* model is regarded to be most centric. All these fluids satisfy the empirical link

between $s_{\mathrm{ex,crit}} \approx -k_{\mathrm{B}}$ and $\omega \approx 0$. On the contrary, Mie n-6 fluids show an independent linear relationship between $s_{\mathrm{ex,crit}}$ and ω, revealing their intrinsic limit to represent the essence of a centric particle. This conclusion aligns with a recent work by Paterson et al.[73] who use the curvature of the Zeno line to test the representability of generic potential models.

The comparability between the repulsive and attractive potential contributions to the excess entropy manifests well the structural characteristics of the centric fluid. The radial distribution function of the most centric square-well fluids ($\lambda \approx 1.8$) shows a discontinuity at the distance between the first and second coordination shells, maximizing the magnitude of multi-particle interaction contribution to the excess entropy. Likewise, the two-body *ab initio* potential shows a steep increase of the multi-particle excess entropy across the critical density, which is interpreted as a result of the harmonization between hard-core and attractive potential contributions.

In addition to these theoretical findings, we expect that the physical insight obtained in this work would be beneficial from an industrial point of view, considering the prevalent use of the acentric factor for modeling the thermodynamic and transport properties of fluids. For instance, they can be used to determine a suitable model potential or the exponent of the repulsive/attractive potentials for coarse-grained modeling of globular molecules or molecular thermodynamic EOSs. The direct link between the excess entropy and centricity can also work as a basis to test the physical adequateness of an arbitrary EOS and an *ab initio*-derived model potential.

SUPPLEMENTARY MATERIAL

Supplementary Material provides additional details, which include classical ^{4}He excess entropy calculation results, van der Waals method to estimate the gas-liquid critical point, two-phase molecular dynamics and Monte Carlo simulation results, test of the excess entropy calculation algorithms, critical point and acentric factor calculation results, and thermodynamic and structural properties data.

ACKNOWLEDGMENTS

The authors thank Allan H. Harvey for stimulating discussions. T. Yoon acknowledges a generous support by the Ministry of Education of the Republic of Korea and the National Research Foundation of Korea (NRF-RS-2023-00273178).

AUTHOR DECLARATIONS

Conflict of Interest

The authors have no conflicts to disclose.

Author Contributions

Tae Jun Yoon: Conceptualization; Methodology; Software; Validation; Formal analysis; Investigation; Resources; Data Curation; Writing - Original Draft; Writing - Review & Editing; Visualization; Project administration; Funding acquisition.
Ian H. Bell: Conceptualization; Methodology; Software; Validation; Formal analysis; Investigation; Writing - Review & Editing.

DATA AVAILABILITY

Data are available in article, Supplementary Material, and one of the authors' code repository (https://github.com/tyoon124/bell2023centricity).

REFERENCES

[1]J. M. Smith, H. C. Van Ness, M. M. Abbott, and M. T. Swihart, *Introduction to chemical engineering thermodynamics, 8th Ed.* (McGraw-Hill, New York, 2017).
[2]J. H. Hildebrand, "The Entropy of Vaporization as a Means of Distinguishing Normal Liquids," J. Am. Chem. Soc. **37**, 970–978 (1915).
[3]K. S. Pitzer, "Corresponding states for perfect liquids," J. Chem. Phys. **7**, 583–590 (1939).
[4]E. A. Guggenheim, "The principle of corresponding states," J. Chem. Phys. **13**, 253–261 (1945).

[5]K. S. Pitzer, D. Z. Lippmann, R. Curl Jr, C. M. Huggins, and D. E. Petersen, "The Volumetric and Thermodynamic Properties of Fluids. II. Compressibility Factor, Vapor Pressure and Entropy of Vaporization," J. Am. Chem. Soc. **77**, 3433–3440 (1955).

[6]K. S. Pitzer, "Origin of the Acentric Factor," in *Phase Equilibria and Fluid Properties in the Chemical Industry*, Vol. 60 (ACS Publications, Washington, DC, 1993) Chap. 1, pp. 1–10.

[7]J. D. Weeks, D. Chandler, and H. C. Andersen, "Role of repulsive forces in determining the equilibrium structure of simple liquids," J. Chem. Phys. **54**, 5237–5247 (1971).

[8]E. W. Lemmon, I. H. Bell, M. L. Huber, and M. O. McLinden, "NIST Standard Reference Database 23: Reference Fluid Thermodynamic and Transport Properties-REFPROP, Version 10.0, National Institute of Standards and Technology," (2018).

[9]J. C. Dyre, "Perspective: Excess-entropy scaling," J. Chem. Phys. **149**, 210901 (2018).

[10]I. H. Bell and A. Jäger, "Calculation of critical points from Helmholtz-energy-explicit mixture models," Fluid Phase Equilib. **433**, 159–173 (2017).

[11]I. H. Bell, G. Galliero, S. Delage-Santacreu, and L. Costigliola, "An entropy scaling demarcation of gas-and liquid-like fluid behaviors," J. Chem. Phys. **152**, 191102 (2020).

[12]T. J. Yoon, M. Y. Ha, E. A. Lazar, W. B. Lee, and Y.-W. Lee, "Topological extension of the isomorph theory based on the Shannon entropy," Phys. Rev. E **100**, 012118 (2019).

[13]I. H. Bell, "Effective hardness of interaction from thermodynamics and viscosity in dilute gases," J. Chem. Phys. **152**, 164508 (2020).

[14]I. H. Bell, S. Delage-Santacreu, H. Hoang, and G. Galliero, "Dynamic crossover in fluids: From hard spheres to molecules," J. Phys. Chem. Lett. **12**, 6411–6417 (2021).

[15]S. Khrapak, "Gas–liquid crossover in the Lennard-Jones system," J. Chem. Phys. **156**, 116101 (2022).

[16]I. H. Bell, "Entropy Scaling of Viscosity—II: Predictive Scheme for Normal Alkanes," J. Chem. Eng. Data **65**, 5606–5616 (2020).

[17]A. N. Singh, J. C. Dyre, and U. R. Pedersen, "Solid–liquid coexistence of neon, argon, krypton, and xenon studied by simulations," J. Chem. Phys. **154**, 134501 (2021).

[18]T. J. Yoon, L. A. Patel, T. Ju, M. J. Vigil, A. T. Findikoglu, R. P. Currier, and K. A. Maerzke, "Thermodynamics, dynamics, and structure of supercritical water at extreme conditions," Phys. Chem. Chem. Phys. **22**, 16051–16062 (2020).

[19]K. S. Pitzer, "The Volumetric and Thermodynamic Properties of Fluids. I. Theoretical Basis and Virial Coefficients," J. Am. Chem. Soc. **77**, 3427–3433 (1955).

[20]I. H. Bell, "Entropy Scaling of Viscosity—I: a Case Study of Propane," J. Chem. Eng. Data **65**, 3203–3215 (2020).

[21]I. H. Bell, R. Fingerhut, J. Vrabec, and L. Costigliola, "Connecting entropy scaling and density scaling," J. Chem. Phys. **157**, 074501 (2022).

[22]D. Fragiadakis and C. Roland, "Connection between dynamics and thermodynamics of liquids on the melting line," Phys. Rev. E **83**, 031504 (2011).

[23]R. V. Vaz, A. L. Magalhães, D. L. Fernandes, and C. M. Silva, "Universal correlation of self-diffusion coefficients of model and real fluids based on residual entropy scaling law," Chem. Eng. Sci. **79**, 153–162 (2012).

[24]A. Dehlouz, J.-N. Jaubert, G. Galliero, M. Bonnissel, and R. Privat, "Combining the entropy-scaling concept and cubic-or SAFT equations of state for modelling thermal conductivities of pure fluids," Int. J. Heat Mass Transf. **196**, 123286 (2022).

[25]R. A. Messerly, N. Gokul, A. J. Schultz, D. A. Kofke, and A. H. Harvey, "Molecular Calculation of the Critical Parameters of Classical Helium," J. Chem. Eng. Data **65**, 1028–1037 (2019).

[26]U. K. Deiters and R. J. Sadus, "Ab Initio Interatomic Potentials and the Classical Molecular Simulation Prediction of the Thermophysical Properties of Helium," J. Phys. Chem. B **124**, 2268–2276 (2020).

[27]J. G. Kirkwood, "Critique of the free volume theory of the liquid state," J. Chem. Phys. **18**, 380–382 (1950).

[28]J. Hirschfelder, D. Stevenson, and H. Eyring, "A Theory of Liquid Structure," J. Chem. Phys. **5**, 896–912 (1937).

[29]M. G. Noro and D. Frenkel, "Extended corresponding-states behavior for particles with variable range attractions," J. Chem. Phys. **113**, 2941–2944 (2000).

[30]B. Widom, "Some topics in the theory of fluids," J. Chem. Phys. **39**, 2808–2812 (1963).

[31]S. Toxvaerd, "Role of attractive forces in determining the equilibrium structure and dynamics of simple liquids," Condens. Matter Phys. **18**, 13002 (2015).

[32]S. Asakura and F. Oosawa, "On interaction between two bodies immersed in a solution of macromolecules," J. Chem. Phys. **22**, 1255–1256 (1954).

[33]N. F. Carnahan and K. E. Starling, "Equation of state for nonattracting rigid spheres," J. Chem. Phys. **51**, 635–636 (1969).

[34]J. R. Mick, M. Soroush Barhaghi, B. Jackman, K. Rushaidat, L. Schwiebert, and J. J. Potoff, "Optimized Mie potentials for phase equilibria: Application to noble gases and their mixtures with n-alkanes," J. Chem. Phys. **143**, 114504 (2015).

[35]E. Vogel, B. Jäger, R. Hellmann, and E. Bich, "Ab initio pair potential energy curve for the argon atom pair and thermophysical properties for the dilute argon gas. II. Thermophysical properties for low-density argon," Mol. Phys. **108**, 3335–3352 (2010).

[36]B. Jäger, R. Hellmann, E. Bich, and E. Vogel, "State-of-the-art ab initio potential energy curve for the krypton atom pair and thermophysical properties of dilute krypton gas," J. Chem. Phys. **144**, 114304 (2016).

[37]R. Hellmann, B. Jäger, and E. Bich, "State-of-the-art ab initio potential energy curve for the xenon atom pair and related spectroscopic and thermophysical properties," J. Chem. Phys. **147**, 034304 (2017).

[38]D. Henderson, "Rowlinson's Concept of an Effective Hard Sphere Diameter," J. Chem. Eng. Data **55**, 4507–4508 (2010).

[39]E. Attia, J. C. Dyre, and U. R. Pedersen, "Comparing four hard-sphere approximations for the low-temperature WCA melting line," J. Chem. Phys. **157**, 034502 (2022).

[40]M. N. Bannerman, R. Sargant, and L. Lue, "DynamO: a free $\mathcal{O}$(N) general event-driven molecular dynamics simulator," J. Comput. Chem. **32**, 3329–3338 (2011).

[41]M. G. Martin, "MCCCS Towhee: a tool for Monte Carlo molecular simulation," Mol. Simul. **39**, 1212–1222 (2013).

[42]E. A. Muller, Å. Ervik, and A. Mejía, "A guide to computing interfacial properties of fluids from molecular simulations [Article v1.0]," Living J. Comp. Mol. Sci. **2**, 21385–21385 (2020).

[43]A. P. Thompson, H. M. Aktulga, R. Berger, D. S. Bolintineanu, W. M. Brown, P. S. Crozier, P. J. in't Veld, A. Kohlmeyer, S. G. Moore, T. D. Nguyen, *et al.*, "LAMMPS-a flexible simulation tool for particle-based materials modeling at the atomic, meso, and continuum scales," Comp. Phys. Comm. **271**, 108171 (2022).

[44]H. Liu, S. Garde, and S. Kumar, "Direct determination of phase behavior of square-well fluids," J. Chem. Phys. **123**, 174505 (2005).

[45]N. M. Tukur, L. V. Woodcock, and L. Lue, "Studies of the Thermodynamic Conditions for the Existence of a Stable Liquid Phase in Square Well Fluids," in *2004 AIChE Annual Meeting*, edited by American Institute of Chemical Engineers (American Institute of Chemical Engineers, Austin, Texas, 2004) pp. 3437–3459.

[46]L. Vega, E. de Miguel, L. F. Rull, G. Jackson, and I. A. McLure, "Phase equilibria and critical behavior of square-well fluids of variable width by Gibbs ensemble Monte Carlo simulation," J. Chem. Phys. **96**, 2296–2305 (1992).

[47]F. Del Rio, E. Avalos, R. Espindola, L. F. Rull, G. Jackson, and S. Lago, "Vapour—liquid equilibrium of the square-well fluid of variable range via a hybrid simulation approach," Mol. Phys. **100**, 2531–2546 (2002).

[48]J. R. Elliott and L. Hu, "Vapor-liquid equilibria of square-well spheres," J. Chem. Phys. **110**, 3043–3048 (1999).

[49]G. Orkoulas and A. Z. Panagiotopoulos, "Phase behavior of the restricted primitive model and square-well fluids from Monte Carlo simulations in the grand canonical ensemble," J. Chem. Phys. **110**, 1581–1590 (1999).

[50]J. K. Singh, D. A. Kofke, and J. R. Errington, "Surface tension and vapor–liquid phase coexistence of the square-well fluid," J. Chem. Phys. **119**, 3405–3412 (2003).

[51]E. de Miguel, "Critical behavior of the square-well fluid with λ= 2: A finite-size-scaling study," Phys. Rev. E **55**, 1347 (1997).

[52]T. J. Yoon, M. Y. Ha, W. B. Lee, and Y.-W. Lee, "Probabilistic characterization of the Widom delta in supercritical region," J. Chem. Phys. **149**, 014502 (2018).

[53]S. Sastry, D. S. Corti, P. G. Debenedetti, and F. H. Stillinger, "Statistical geometry of particle packings. I. Algorithm for exact determination of connectivity, volume, and surface areas of void space in monodisperse and polydisperse sphere packings," Phys. Rev. E **56**, 5524 (1997).

[54]R. Bieshaar, A. Geiger, and N. N. Medvedev, "Calculation of Chemical Potentials by a Novel Delaunay-Simplex Sampling Technique for Particle Insertion," Mol. Simul. **15**, 189–196 (1995).

[55]C. H. Rycroft, "VORO++: A three-dimensional Voronoi cell library in C++," Chaos **19**, 041111 (2009).

[56]C. Hoheisel and U. Deiters, "High pressure molecular dynamics of the partially miscible fluid mixture neon/krypton," Mol. Phys. **37**, 95–109 (1979).

[57]D. C. Wallace, "On the role of density fluctuations in the entropy of a fluid," J. Chem. Phys. **87**, 2282–2284 (1987).

[58]P. Giaquinta and G. Giunta, "About entropy and correlations in a fluid of hard spheres," Physica A **187**, 145–158 (1992).

[59]T. J. Yoon, M. Y. Ha, W. B. Lee, and Y.-W. Lee, "Monte Carlo simulations on the local density inhomogeneities of sub-and supercritical carbon dioxide: Statistical analysis based on the Voronoi tessellation," J. Supercrit. Fluids **119**, 36–43 (2017).

[60]T. J. Yoon, M. Y. Ha, W. B. Lee, and Y.-W. Lee, "Molecular dynamics simulation on the local density distribution and solvation structure of supercritical CO_2 around naphthalene," J. Supercrit. Fluids **130**, 364–372 (2017).

[61]M. W. Maddox, G. Goodyear, and S. C. Tucker, "Origins of Atom-Centered Local Density Enhancements in Compressible Supercritical Fluids," J. Phys. Chem. B **104**, 6248–6257 (2000).

[62]S. Egorov, "Local density augmentation in attractive supercritical solutions: Inhomogeneous fluid approach," J. Chem. Phys. **112**, 7138–7146 (2000).

[63]S. C. Tucker, "Solvent Density Inhomogeneities in Supercritical Fluids," Chem. Rev. **99**, 391–418 (1999).

[64]W. Song, R. Biswas, and M. Maroncelli, "Intermolecular Interactions and Local Density Augmentation in Supercritical Solvation: A Survey of Simulation and Experimental Results," J. Phys. Chem. A **104**, 6924–6939 (2000).

[65]J. Lewis, R. Biswas, A. Robinson, and M. Maroncelli, "Local Density Augmentation in Supercritical Solvents: Electronic Shifts of Anthracene Derivatives," J. Phys. Chem. B **105**, 3306–3318 (2001).

[66]I. Skarmoutsos and J. Samios, "Local density augmentation and dynamic properties of hydrogen-and non-hydrogen-bonded supercritical fluids: A molecular dynamics study," J. Chem. Phys. **126** (2007), 10.1063/1.2431370.

[67]Y. Reyes, C. A. Flores-Sandoval, and P. Orea, "Common behavior of the critical properties of the 2D and 3D square-well fluids," J. Chem. Phys. **139**, 164505 (2013).

[68]H. Okumura and F. Yonezawa, "Liquid–vapor coexistence curves of several interatomic model potentials," J. Chem. Phys. **113**, 9162–9168 (2000).

[69]S. Werth, K. Stöbener, M. Horsch, and H. Hasse, "Simultaneous description of bulk and interfacial properties of fluids by the mie potential," Mol. Phys. **115**, 1017–1030 (2017).

[70]S. Stephan and M. Urschel, "Characteristic curves of the mie fluid," J. Mol. Liq. **383**, 122088 (2023).

[71]M. Thol, G. Rutkai, A. Köster, R. Lustig, R. Span, and J. Vrabec, "Equation of State for the Lennard-Jones Fluid," J. Phys. Chem. Ref. Data **45**, 023101 (2016).

[72]M. P. Bernhardt, Y. Nagata, and N. F. van der Vegt, "Where Lennard-Jones Potentials Fail: Iterative Optimization of Ion–Water Pair Potentials Based on Ab Initio Molecular Dynamics Data," J. Phys. Chem. Lett. **13**, 3712–3717 (2022).

[73]T. Paterson, M. N. Bannerman, and L. Lue, "Using the Zeno line to assess and refine molecular models," J. Chem. Phys. **160**, 154503 (2024).